Research Article

Cong-Man Wang, Xue-Cheng Ping* and Xing-Xing Wang

Effects of local fiber discontinuity on the fatigue strength parameter at the fiber inclusion corner in fiber-reinforced composites

https://doi.org/10.1515/secm-2022-0021 received March 14, 2022; accepted July 03, 2022

Abstract: To comprehend the fatigue failure mechanism at the fiber discontinuity in fiber-reinforced composites, it is necessary to evaluate the local mechanical behaviors. The fatigue strength depends on the stress distribution at the fiber inclusion corner. An improved advanced finite element method (IAFEM) is proposed for the stress intensity factor (SIF) analysis at the fiber inclusion corner. In the IAFEM, the element stiffness matrix of singular inclusion corner element (SICE) is obtained, and the singular elastic field at the tip of the fiber inclusion is determined. The effects of load direction, fiber distribution, fiber geometry, and material properties on SIFs are analyzed numerically using the IAFEM. The difference in stress field distribution between two-dimensional and threedimensional fiber inclusions is discussed. The IAFEIM and calculation results can provide reference for fatigue strength analysis and preparation of composite materials.

Keywords: fatigue strength, fiber-reinforced composite, singular inclusion corner element, stress intensity factor

1 Introduction

Fiber-reinforced composites are utilized in automotive, aerospace, and other engineering fields due to their lightweight, low cost, and high-quality processing performance [1-4]. In composite materials subjected to cyclic loading, the high stress zone prone to crack initiation is usually located at geometric discontinuities due to material mismatch. In fiber-reinforced composites, local fiber fracture is a typical defect [5-7]. The criteria for evaluating the fatigue strength of materials mostly depend on assumed structural models. Fatigue behavior can be evaluated in terms of parameters which are meaningfully significant to fatigue phenomena, such as the common S-N curve which combines design stress with the number of cycles. Generally, the fatigue strength S in the S-N curve is related to the definition of nominal stress [8]. If the root radius of the inclusion corner tip is assumed to be zero, stress singularity will appear in linear elastic analysis. Failure prediction based on stress singularity analysis is an active research topic [9]. Seweryn's criterion of brittle failure is based on whether the average stress for crack initiation or propagation to a specific damage stage reaches the critical value [10]. Although the stress near the stress singularity point tends to be infinite, the energy in the small piece of material around the stress singularity point is finite, thus appropriate characterization parameters are a prerequisite for accurate prediction of fatigue failure. Fatigue tests prove that maximum principal stress can be applied to the prediction of fatigue limit, but the scatter of the experimental data was obvious. Relatively speaking, stress intensity factor (SIF) is used as a meaningful parameter for the prediction of fatigue failure [11].

There have been a lot of research works on the singular stress field analysis and SIF of fiber inclusions in composites. Bogy and Wang [12] first studied the stress field at the corner of cylindrical inclusions. Zbib et al. [13] established an analytical expression of SIF for cylindrical cracks located at the fiber-matrix interface. Jiang et al. [14]

^{*} Corresponding author: Xue-Cheng Ping, School of Mechanical Engineering, Tianjin University of Science and Technology, Tianjin 300222, China; Tianjin Key Laboratory of Integrated Design and Online Monitoring of Light Industry and Food Engineering Machinery and Equipment, Tianjin University of Science and Technology, Tianjin 300222, China, e-mail: xcping@tust.edu.cn
Cong-Man Wang, Xing-Xing Wang: School of Mechanical Engineering, Tianjin University of Science and Technology, Tianjin 300222, China; Tianjin Key Laboratory of Integrated Design and Online Monitoring of Light Industry and Food Engineering Machinery and Equipment, Tianjin University of Science and Technology, Tianjin 300222, China

developed an analytical method for periodic cylindrical inclusions under longitudinal shear by using equivalent inclusion technique and combining the results of Riemann boundary value problem. Bian et al. [15] used Eshelby's equivalent inclusion theory and Mori-Tanaka method to derive an analytical formula for stress distribution near fibers. Mantič [16] studied the plane strain problem of a single cylindrical inclusion embedded in an infinite matrix under uniform uniaxial transverse tension based on the stress criterion of coupling nodes and incremental energy criterion. Vable and Maddi [17] effectively applied the boundary element method for stress analysis of polygonal inclusions. Chen [18] introduced the basic density function in the physical force method to characterize the stress singularity at the inclusion corner in numerical analysis. Noda et al. [19-21] systematically calculated the generalized SIF at the inclusion corner with the body force method. Bulling et al. [22] proposed a finite element method (FEM) for automatic enrichment near stress singularities and constructed a semi-analytical singular mode to evaluate the SIFs in the areas of stress singularities.

Due to the complexity of boundary conditions and governing equations, the analytical method is only suitable for certain models which are relatively simple. The goal of fracture analysis using FEM or other numerical methods is to compute the singular stress at the crack tip or inclusion. Tan and Meguid [23] established a new singular FEM by using the complex function method, which could reliably and effectively determine the singular stress field and the related SIFs for various wedge geometry and elastic mismatches. Liou [24] developed a global-local FEM to predict the stress distributions of short fiber-reinforced composite. Madenci et al. [25] developed finite element analysis combining special and conventional elements to provide an accurate description of the stress field at the interface of two materials or at the junction of different materials. Lei et al. [26] evaluated the micromechanical properties of composite materials reinforced with single and clustered polygonal fibers using the FEM. Zhang and Katsube [27] proposed a new mixed FEM for mechanical analysis of heterogeneous materials with randomly dispersed inclusions. Symplectic singular element is a special singular element in the framework of FEM, which can be used to solve the dynamic SIF of bimaterial interface cracks [28,29]. Chen et al. [30] developed a singular edge smooth FEM to solve crack problems in anisotropic media.

In order to ensure the compatibility of singular elements, it is usually necessary to use transition elements between singular elements and regular elements. However,

Chen and Ping [31] and Ping et al. [32] developed a kind of super singular corner element method based on the special finite element characteristic analysis method, which achieved the consistency degree of freedom between the singular element and the conventional element. By using the characteristic solutions of numerical stress field and displacement field, the singular stress near the tip of polygonal inclusion embedded in the matrix was analyzed by the super singular corner element. The super singular corner element method was further extended to deal with the 3D singular stress field problems [33–35]. The local fiber discontinuity problem is a typical three-dimensional (3D) inclusion problem in fiber-reinforced composites. It is necessary to propose an effective solution method and do more research on the stress singularity problem at the fiber inclusion corner.

In this work, using an ad hoc finite element eigenanalysis method and based on the Hellinger-Reissner (H-R) variational principle, a singular inclusion corner element (SICE) containing a part of cylindrical inclusion corner front is established. By using the SICE method, the singular stress field at the inclusion corner tip of double cylindrical inclusions under different loading conditions is analyzed. The effects of material mismatches, inclusion size, inclusion spacing, and unit cell size on SIF are analyzed. The differences in singular stress fields solved by two-dimensional (2D) and 3D models are compared. Once the fatigue strength judgment parameters are obtained, the numerical analysis results can be used to predict fatigue damage problems at 3D fiber discontinuity position.

2 Quantitative parameters of fatigue strength

Inclusion is the key factor to cause low-cycle fatigue failure. SIF is an important characterization parameter of progressive stress distribution near inclusion corner. The relationship between the SIF and the stress components at the angle bisector of the matrix corner adjacent to the inclusion corner in asymptotic stress field can be approximated as follows:

$$K_{\rm I} = \lim_{\rho \to 0} \sqrt{2} \rho^{-\lambda_{\rm I}} \sigma_{\phi}(\rho, \phi_{\rm b}, \theta), \tag{1}$$

$$K_{\rm II} = \lim_{\rho \to 0} \sqrt{2} \rho^{-\lambda_{\rm II}} \sigma_{\rho \phi}(\rho, \phi_{\rm b}, \theta), \tag{2}$$

$$K_{\rm III} = \lim_{\rho \to 0} \sqrt{2} \rho^{-\lambda_{\rm III}} \sigma_{\phi\theta}(\rho, \phi_{\rm b}, \theta), \tag{3}$$

where ϕ_b is the angle ϕ located at the angle bisector of the matrix corner as shown in Figure 2a. For singular stress field analysis, $\rho = 0.0001R$. The values of characteristic roots λ_I , λ_{II} , and λ_{III} are related to material properties and inclusion shape [36].

For comparative analysis of 2D and 3D models, the dimensionless SIFs are expressed as:

$$F_{\rm I} = \lim_{\rho \to 0} \frac{\rho^{-\lambda_{\rm I}} \sigma_{\phi}(\rho, \phi_{\rm b}, \theta)}{\sigma^{\infty} R^{-\lambda_{\rm I}} \sqrt{\pi} f_{\phi_{\rm b}, I}^{\rm I}},\tag{4}$$

$$F_{\rm II} = \lim_{\rho \to 0} \frac{\rho^{-\lambda_{\rm II}} \sigma_{\rho\phi}(\rho, \phi_{\rm b}, \theta)}{\sigma^{\infty} R^{-\lambda_{\rm II}} \sqrt{\pi} f_{\phi_{\rm b}, I}^{\rm II}}, \tag{5}$$

$$F_{\text{III}} = \lim_{\rho \to 0} \frac{\rho^{-\lambda_{\text{III}}} \sigma_{\rho\theta}(\rho, \phi_{\text{b}}, \theta)}{\sigma^{\text{co}} R^{-\lambda_{\text{III}}} \sqrt{\pi} f_{\phi_{\text{b}},I}^{\text{III}}}, \tag{6}$$

where specific expressions of $f_{\phi_b,I}^{\rm I}$, $f_{\phi_b,I}^{\rm II}$, and $f_{\phi_b,I}^{\rm III}$ can be referred from ref. [21].

3 SICE model for a cylindrical inclusion corner

In this section, based on the numerical eigen solutions of singular stress field and the generalized H–R variational principle, an SICE is established, and its validity is verified.

3.1 Establishment of the SICE model

In Figure 1a, we assume that 3D cylindrical inclusions are located in the matrix. To analyze the singular stress field at the corner of the inclusion, a unit cell containing a cylindrical inclusion is established, as shown in Figure 1b. 2H is the height of the unit cell, 2W is its length, and 2B is its width. If there are no special instructions, it is assumed that H = W = B.

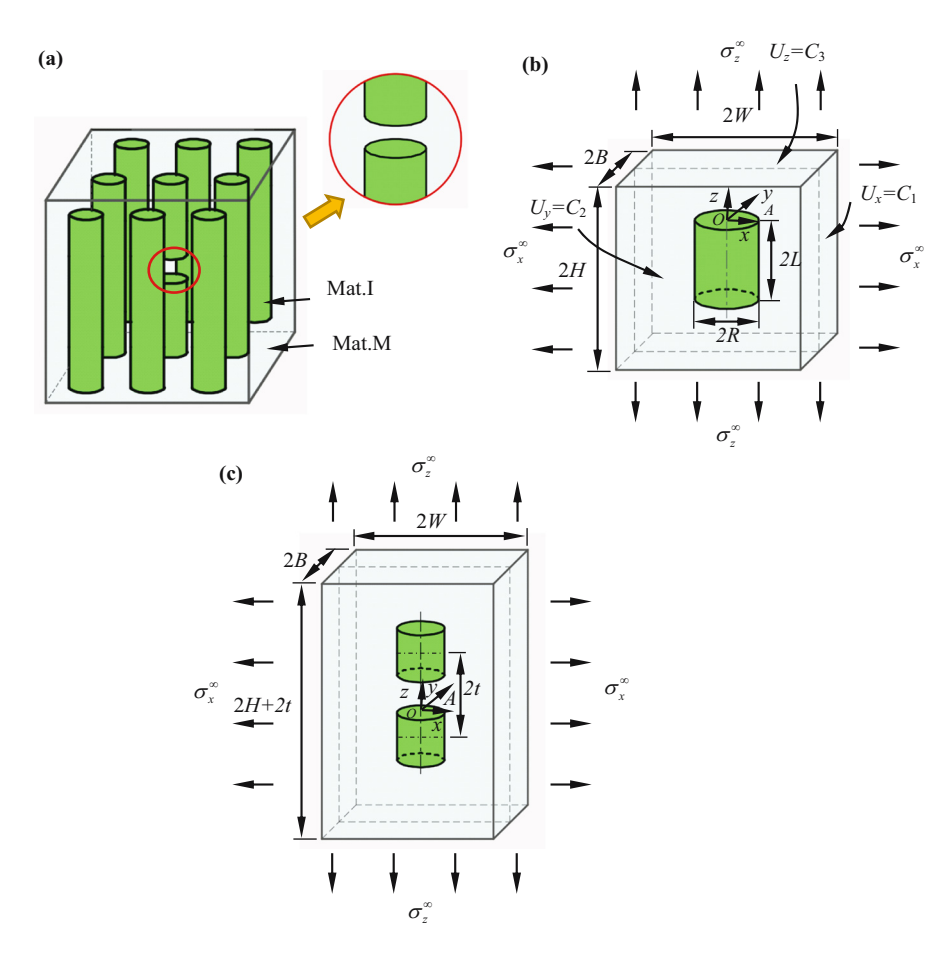
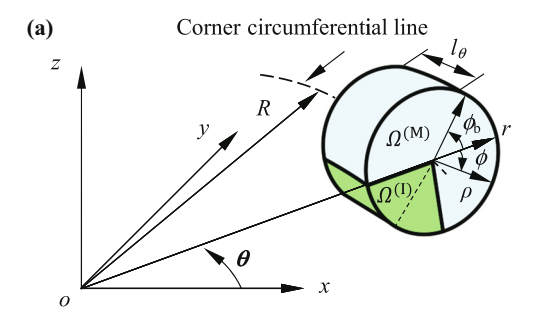


Figure 1: (a) Periodic inclusion model with a local fiber discontinuity; (b) a cylindrical inclusion in a unit cell model; and (c) two cylindrical inclusions aligned in the z-direction.



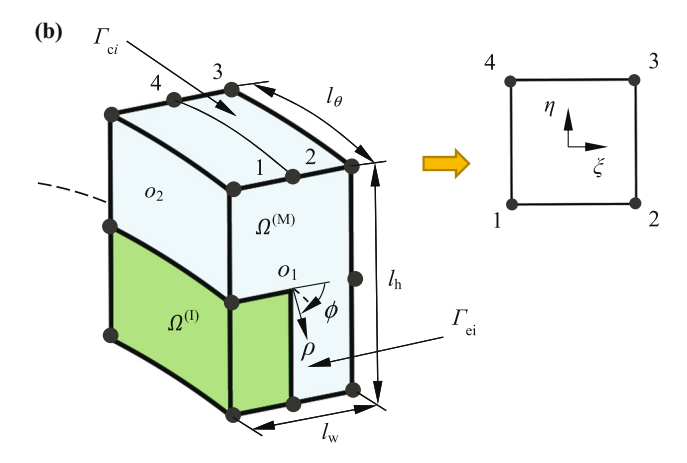


Figure 2: Definition of a SICE along the inclusion corner line: (a) Local curvilinear coordinate in rectangular coordinate and cylindrical coordinate; and (b) SICE containing partial inclusion corner line.

The diameter of the cylindrical inclusion is 2R and the height is 2L. The boundary condition of the unit cell satisfies $U_x = C_1$, $U_y = C_2$, and $U_z = C_3$. That is, the six planes are translational in the loading process. The elasticity modulus of the inclusion and the matrix are E_I and E_M , respectively. The Poisson's ratios are v_I and v_M , respectively. Taking the center point O of the top surface of the cylindrical inclusion as the origin point, the Cartesian coordinate system is established to obtain the singular stress field near the inclusion corner line A. As shown in Figure 2a, a local coordinate system (ρ, ϕ, θ) is established with a point on the inclusion corner front line A. In the region where $\rho \ll R$, the asymptotic displacement and stress on the angular bisector of the cylindrical inclusion corner can be expressed as follows:

$$u_i(\rho, \phi, \theta) = \operatorname{Re} \left[\sum_{n=1}^{N+M} \rho^{\lambda_n + 1} u_i^{(n)}(\phi, \theta) \beta_n \right], \tag{7}$$

$$\sigma_{ij}(\rho, \phi, \theta) = \mathbf{D} \operatorname{Re} \left\{ \sum_{n=1}^{N+M} \rho^{\lambda_n} \varepsilon_{ij}^{(n)}(\phi, \theta) \beta_n \right\}, \quad (8)$$

where λ is the characteristic root of the characteristic equation [37]. The number of intercepted characteristic

roots may be multiple, which may be real or complex. N is the number of intercepted complex roots, and M is the number of intercepted real roots. Due to the bounded strain energy, only the eigen values within the range of $\text{Re}(\lambda) > -1$ are considered herein. \mathbf{D} is the elastic matrix of the material, and β_n is the stress intensity coefficient to be solved.

The displacement and stress field in the global coordinate system (x, y, z) can be obtained by transforming the corresponding parameters in the local coordinate system (ρ, ϕ, θ) , i.e.,

$$\mathbf{u}(x, y, z) = \mathbf{T}_{11}\mathbf{u}(\rho, \phi, \theta) = \mathbf{T}_{11}\mathbf{U}\boldsymbol{\beta}, \tag{9}$$

$$\mathbf{\sigma}(x, y, z) = \mathbf{D}\mathbf{T}_{\varepsilon}\mathbf{\varepsilon}(\rho, \phi, \theta) = \mathbf{D}\mathbf{T}_{\varepsilon}\mathbf{E}\boldsymbol{\beta}, \tag{10}$$

in which

$$\boldsymbol{U} = [\hat{\mathbf{u}}^{(1)} \cdots \hat{\mathbf{u}}^{(N)} \ \mathbf{u}^{(N+1)}(\rho, \phi, \theta) \cdots \mathbf{u}^{(N+M)}(\rho, \phi, \theta)], \quad (11)$$

$$\mathbf{E} = [\hat{\boldsymbol{\varepsilon}}^{(1)} \cdots \hat{\boldsymbol{\varepsilon}}^{(N)} \boldsymbol{\varepsilon}^{(N+1)}(\rho, \phi, \theta) \cdots \boldsymbol{\varepsilon}^{(N+M)}(\rho, \phi, \theta)], \quad (12)$$

$$\boldsymbol{\beta} = [\hat{\boldsymbol{\beta}}_1^T \cdots \hat{\boldsymbol{\beta}}_N^T \beta_{N+1} \cdots \beta_{N+M}]^T.$$
 (13)

In Figure 2b, an SICE containing partial inclusion corner line is established. The singular element contains the inclusion domain $\Omega^{\rm I}$ and the matrix domain $\Omega^{\rm M}$. $\Gamma_{\rm ei}$ is the end surface of the SICE. $\Gamma_{\rm ci}$ is the remaining surface of the SICE. In order to solve the unknown parameter β_n according to the H–R variational principle, the variational functional at the inclusion corner is defined as follows:

$$\prod_{H-R} = -\frac{1}{2} \sum_{k=I,M} \int_{\Gamma_{c}^{(I)}} \sigma_{ij}^{(k)}(x,y,z) n_{j} u_{i}^{(k)}(x,y,z) d\Gamma
+ \sum_{k=I,M} \int_{\Gamma_{c}^{(I)}} \sigma_{ij}^{(k)}(x,y,z) n_{j} \bar{u}_{i}^{(k)}(x,y,z) d\Gamma,$$
(14)

By solving the steady state value of the functional, the element stiffness matrix of the SICE is established, and the singular stress field at the inclusion corner is obtained.

$$\mathbf{K}_{c} = \mathbf{G}^{\mathrm{T}} \mathbf{H}^{-1} \mathbf{G}, \tag{15}$$

$$\mathbf{H} = \frac{1}{2} \int_{\Gamma_c} [(\mathbf{n} \ \mathbf{E}_c)^T \mathbf{U}_c + (\mathbf{U}_c)^T (\mathbf{n} \ \mathbf{E}_c)] dA, \tag{16}$$

$$\mathbf{G} = \int_{\Gamma} (\mathbf{n} \mathbf{E}_{c})^{T} \mathbf{N}_{h} dA, \tag{17}$$

$$\mathbf{U}_{c} = [(1 - \eta)\mathbf{T}_{u}\mathbf{U}/2 \ (1 + \eta)\mathbf{T}_{u}\mathbf{U}/2], \tag{18}$$

$$\mathbf{E}_{c} = [(1 - \eta)\mathbf{D}\mathbf{T}_{\varepsilon}\mathbf{E}/2 \ (1 + \eta)\mathbf{D}\mathbf{T}_{\varepsilon}\mathbf{E}/2], \tag{19}$$

where Γ_c is the assembly of Γ_{ci} , \boldsymbol{n} is the unit normal vector, and \boldsymbol{N}_h is the interpolation function matrix.

$$\begin{split} \sigma_{ij}(\rho,\phi_{\mathrm{b}},\theta) &= \frac{(1-\eta)}{2} \cdot \mathrm{Re} \left[\sum_{n=1}^{3} \rho^{\lambda_{n}} D_{ijkl} \varepsilon_{kl}^{(n)}(\phi,\theta) c_{1}^{(n)} \right] \\ &+ \frac{(1+\eta)}{2} \cdot \mathrm{Re} \left[\sum_{n=1}^{3} \rho^{\lambda_{n}} D_{ijkl} \varepsilon_{kl}^{(n)}(\phi,\theta) c_{2}^{(n)} \right]. \end{split} \tag{20}$$

3.2 Verification of the SICE model

In order to verify the SICE model, the unit cell model as shown in Figure 1b is considered. Under the applied load σ_z^{∞} , the stresses $\sigma_{\phi}(\rho, \phi_{\rm b}, \theta)/\sigma_z^{\infty}$ and $\sigma_{\rho\phi}(\rho, \phi_{\rm b}, \theta)/\sigma_z^{\infty}$ on the bisector of the corner of the cylindrical inclusion end are analyzed. The value of ρ varies from 0.0001R to 0.001R. The size of the cylindrical inclusion is L/R = 1. The size of the unit cell is H/L = B/R = W/R = 100. As shown in Figure 3a, due to the symmetry of the structure, a quarter of the model within the range of x > 0 and y > 0is taken for analysis. A 16-node SICE is used at the inclusion corner. The circumferential dimensions and sectional dimensions of the element are as follows: $l_{\theta} = \pi R/80$, $l_{\rm w} = l_{\rm h} = 0.02R$. In order to ensure the high accuracy of calculation, 40 SICEs are set up at the corner of the cylindrical inclusion. They are assembled directly with the surrounding conventional 8-node elements. The type of the conventional 8-node elements is C3D8R and the SICEs are user-defined elements. Singular elements have good compatibility with traditional elements due to the consistent degrees of freedom at element nodes. Under the same condition, the traditional FEM is used to analyze the singular stresses at the inclusion corner, as

shown in Figure 3b. In the range of $0.02R \times 0.02R$, 3,362 elements are used in the traditional finite element model. In contrast, traditional finite element modeling is more complex. Table 1 demonstrates the number of elements and CPU running time analyzed by the SICE method and the traditional FEM. The comparison shows that the SICE model has higher computational efficiency. Figure 4a and b shows the variation in singular stress field parameters $\sigma_{\phi}(0.0001R, \phi_{\rm b}, \theta)/\sigma_z^{\infty}$ and $\sigma_{\rho\phi}(0.0001R, \phi_{\rm b}, \theta)/\sigma_z^{\infty}$ vs ρ/R in the vicinity of the inclusion corner in the unit cell under tensile loading σ_z^{∞} .

Figure 4c and d shows the variation in the singular stress components $\sigma_{\phi}(0.0001R, \phi_{\rm b}, \theta)/\sigma_{\rm x}^{\infty}$ and $\sigma_{\rho\phi}(0.0001R, \phi_{\rm b}, \theta)/\sigma_{\rm x}^{\infty}$ under tensile loading $\sigma_{\rm x}^{\infty}$. By comparison, it is found that the stresses calculated by SICE method is consistent with the stress calculated by traditional FEM, and the maximum error is less than 3.130%.

In the stress intensity coefficient expression, the effect of $Dim(\boldsymbol{\beta}) = (2N + M)$ on the singular stress field of a cylindrical inclusion is shown in Table 2. When Dim $(\boldsymbol{\beta}) = 10-26$, the errors of $\sigma_{\phi}(0.0001R, \phi_{\rm b}, \theta)/\sigma_z^{\infty}$ and $\sigma_{\rho\phi}(0.0001R, \phi_{\rm b}, \theta)/\sigma_z^{\infty}$ are less than 3.128% compared with those obtained by Noda (19), indicating that the SICE method has good convergence.

Table 1: The number of elements and CPU running time for SICE method and traditional FEM (Case in Figure 1b)

L/H	Num. of el	ements	CPU time		
	SICE + FEM	FEM	SICE + FEM	FEM	
L/H = 0.8	61,688	167,442	0:01:48	0:05:53	
L/H = 0.67	66,350	196,361	0:02:05	0:07:03	
L/H = 0.5	80,864	254,736	0:02:21	0:08:07	
L/H = 0.33	89,027	267,255	0:02:31	0:08:13	
L/H = 0.1	105,094	282,590	0:02:58	0:10:13	

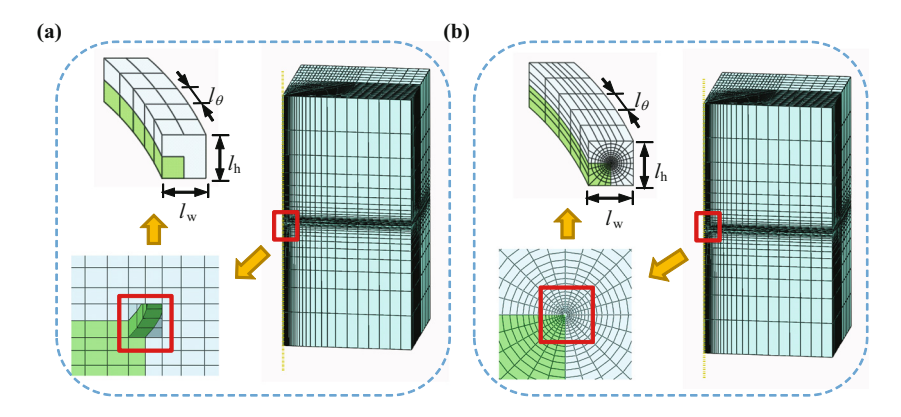


Figure 3: The meshes at the corner of 3D cylindrical inclusion as shown in Figure 1b (L/R = 1, H/L = 100): (a) the mesh using traditional elements and SICEs and (b) the mesh using traditional elements.

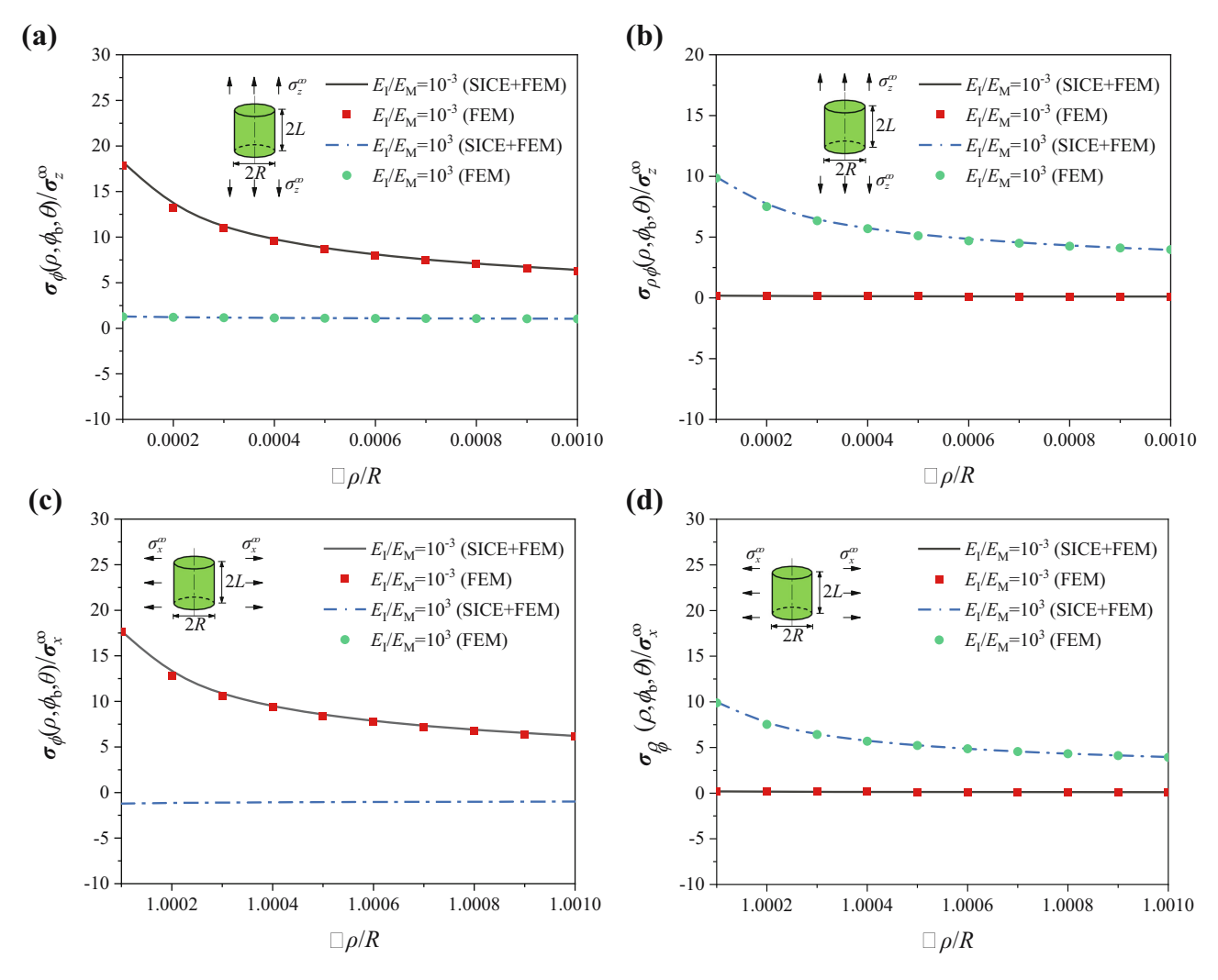


Figure 4: Comparison of stress results between the SICE method and the traditional FEM = (L/R = 1, L/H = 100): (a) and (b) results under tensile loading σ_x^{∞} and (c) and (d) results under tensile loading σ_x^{∞} .

4 Discussion of results

This section applies the SICE model to calculate the fiber inclusion problem under the loading as shown in Figure 1.

The effects of load direction, fiber spacing, fiber geometry, and material properties on SIFs at the inclusion corner are analyzed numerically.

Table 2: Effect of $Dim(\beta) = (2N + M)$ on singular stress field under tensile loading σ_z^{∞} (H/L = 100, L/R = 1)

Dim(β) = 2N + M	$\sigma_{\phi}(0.0001R$	$(\boldsymbol{\phi}_{b},\boldsymbol{\theta})/\sigma_{z}^{\infty}$	$\sigma_{\! ho\phi}(0.0001R, \phi_{ m b}, heta)/\sigma_{ m z}^{\infty}$		
	$\overline{E_{\rm I}/E_{\rm M}}=10^{-2}$	$E_{\rm I}/E_{\rm M}=10^2$	$\overline{E_{\rm I}/E_{\rm M}=10^{-2}}$	$E_{\rm I}/E_{\rm M}=10^2$	
10	15.827	0.193	1.177	8.028	
14	15.892	0.193	1.179	8.092	
18	15.986	0.195	1.183	8.092	
22	15.988	0.195	1.184	8.093	
26	15.987	0.195	1.185	8.090	

4.1 Effects of inclusion size and spacing on the fatigue strength parameters

In the unit cell model as shown in Figure 1b, the effects of inclusion size and spacing on the SIF at corner line A under tensile loading σ_z^∞ are analyzed. A unit cell is considered to be an approximate simulation of periodic inclusions distribution. Let L/H vary from 0.1 to 0.8, variation in SIFs at the inclusion corner with the geometrical parameter L/H is shown in Figure 5. When $E_{\rm I}/E_{\rm M}<1$ (soft inclusion), $K_{\rm I}$ decreases with L/H by 22.466%.

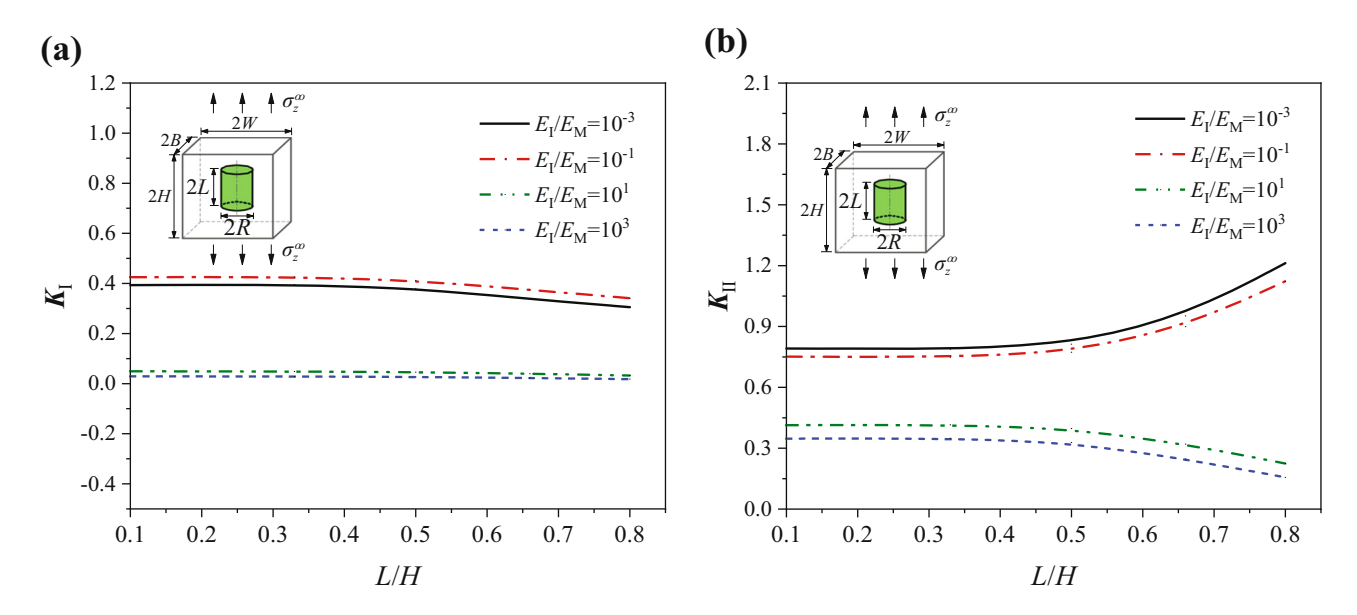


Figure 5: Variation in SIFs at the inclusion corner with the geometrical parameter L/H (L/R = 1) in (a) K_1 and (b) K_{11} .

 $K_{\rm II}$ increases with L/H by 53.176%. When $E_{\rm I}/E_{\rm M} > 1$ (hard inclusion), $K_{\rm I}$ remains unchanged with L/H. $K_{\rm II}$ decreases with L/H by 54.988%. The variation in the analysis results is considered to be caused by the influence of the nearby inclusion.

In order to analysis the influence of fiber fracture, the model of double inclusions aligned in the z-direction is established, as shown in Figure 1c. Let L/H = 0.01, which makes the model approximate to an inclusion in an infinite solid. The z-direction distance between the two inclusions is represented by 2t. As shown in Figure 6, K_1

decreases with L/t for both the soft and hard inclusions. For soft inclusions, $K_{\rm II}$ increases with the increase in the distance 2t between the two inclusions. While for hard inclusions, K_{α} is basically stable after a little decrease with increase in the distance 2t. The extrema of $K_{\rm II}$ when $E_{\rm I}/E_{\rm M}=10^1$ and $E_{\rm I}/E_{\rm M}=10^{-1}$ both appear at L/t=0.7, their values are 0.463 and 0.402, respectively. The results show that the interference of inclusions aligned in the z-direction reduces the tendency of opening fracture at the corner front of the inclusion under tensile loading σ_z^{∞} . The increase in spacing parameter L/t leads to a

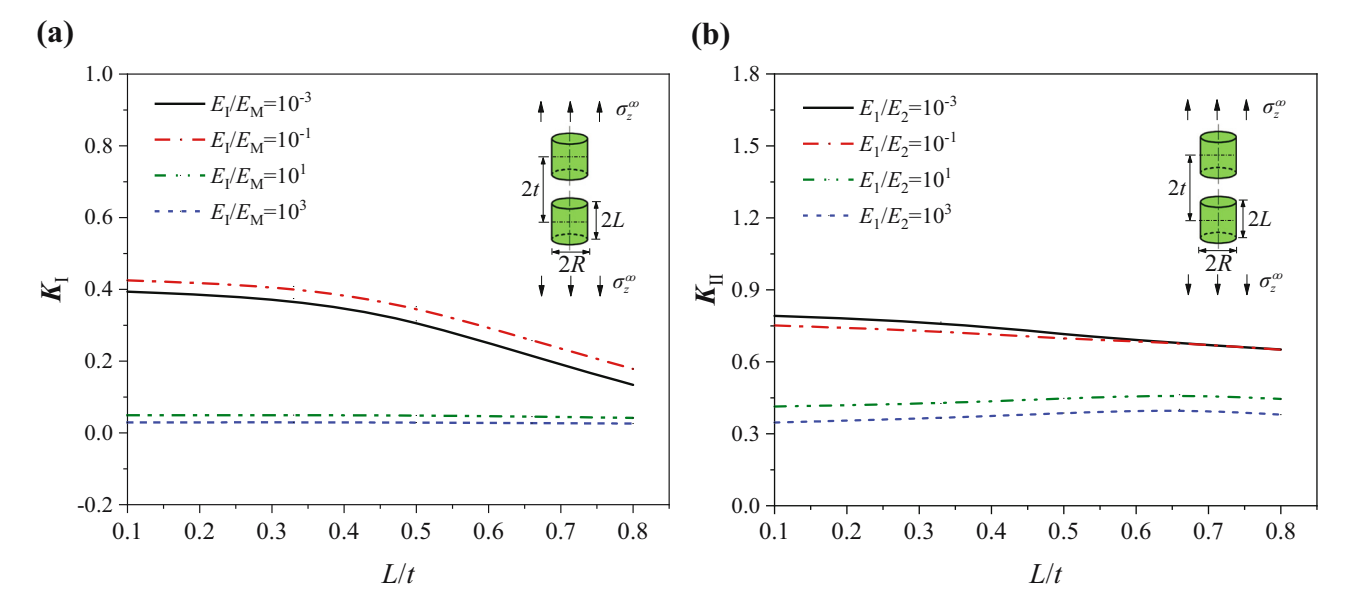


Figure 6: (a) K_{I} and (b) K_{II} in the interaction of double cylindrical inclusions aligned in the z-direction (L/R = 1).

decreasing trend of sliding fracture mode for soft inclusions, while for hard inclusions, the situation is just opposite.

Figure 7 shows $K_{\rm I}$ and $K_{\rm II}$ in the interaction of double inclusions aligned in the *z*-direction and at the corner of an inclusion in a unit cell when L/R = 10. By comparing Figure 7 with Figures 5 and 6, $K_{\rm I}$ is basically the same under tensile loading σ_z^{∞} as L/t or L/H changes when L/R > 10, as opening fracture mode can be observed.

In the current analysis, when $E_I/E_M = 10^{-3}$, the length-diameter ratio (L/R) of the inclusion in the unit cell increases, a decreasing trend corresponding to the two cases L/R = 1 and 10, K_I decreased by 24.834 and 2.969%, respectively.

4.2 Effects of length-diameter ratio and size of a unit cell on fatigue strength parameters

Figure 8a and b shows the variation in $K_{\rm I}$ and $K_{\rm II}$ at the corner A with the length-diameter ratio and size of unit cell under the loading σ_z^{∞} . When $E_{\rm I}/E_{\rm M}=10^3$ and L/R=10, $K_{\rm I}$ and $K_{\rm II}$ increase with W/R, and in most cases decrease with H/L. When H/L>10, the analysis results tend to be consistent, which can be considered as the approximate situation of $H/L\to\infty$. Figure 8c and d shows $K_{\rm I}$ and $K_{\rm II}$ at the corner A of the inclusion when $E_{\rm I}/E_{\rm M}=10^{-3}$. $K_{\rm I}$ and $K_{\rm II}$ decrease with W/R, and in most cases increase with

H/L. This variation trend is contrary to that when $E_{\rm I}/E_{\rm M}=10^3$.

4.3 The fatigue strength parameter results under loading σ_x^{∞}

The variation in $K_{\rm I}$ and $K_{\rm II}$ with L/H of the cylindrical inclusion in a unit cell under tensile loading σ_{χ}^{∞} is shown in Figure 9. Compared with $K_{\rm II}$, the size parameter L/H has less effect on $K_{\rm I}$. The maximum change rate of $K_{\rm I}$ is 10.183%. For soft inclusions, $K_{\rm II}$ increases with L/H by 63.119%. For hard inclusions, $K_{\rm II}$ decreases with L/H by 46.001%. As shown in Figure 10, the variation trend of $K_{\rm I}$ and $K_{\rm II}$ with L/t at the corner of double cylindrical inclusions aligned in the z-direction under σ_{χ}^{∞} is almost opposite to the analysis results under tensile loading σ_{z}^{∞} . An increasing L/t leads to a decreasing trend of sliding fracture mode for hard inclusions, while for soft inclusions, the situation is just opposite.

As shown in Figure 11, under σ_x^{∞} and when B = W, K_1 at the hard inclusion corner in the unit cell is generally small, which means that the possibility of opening fracture mode is small. K_{II} increases with W/R, and the possibility of sliding fracture mode increases. The K_1 and K_{II} at soft inclusion corner in a unit cell increase with W/R in most cases, and the possibility of crack initiation increases. Therefore, the SIF at the corner front of the unit cell is affected by the inclusion material, length-diameter ratio of the inclusion, and size of the unit cell.

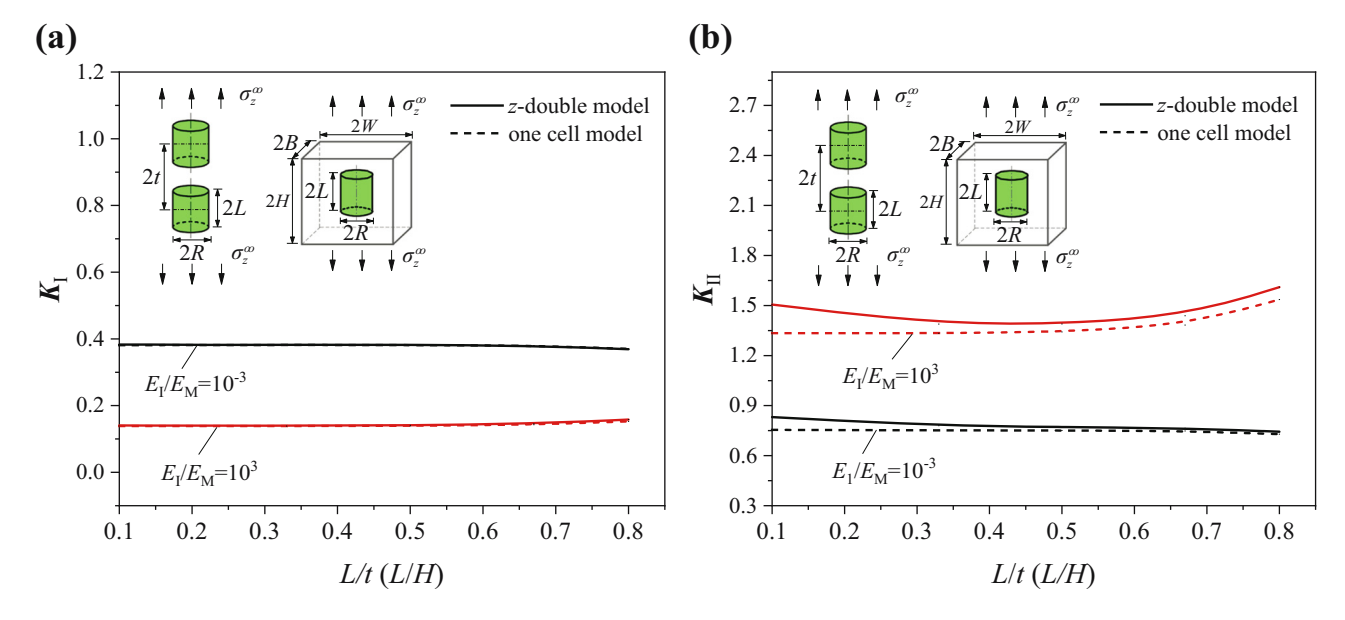


Figure 7: (a) K_1 and (b) K_1 at the corner of double cylindrical inclusions aligned in the z-direction and inclusion in unit cell (L/R = 10).

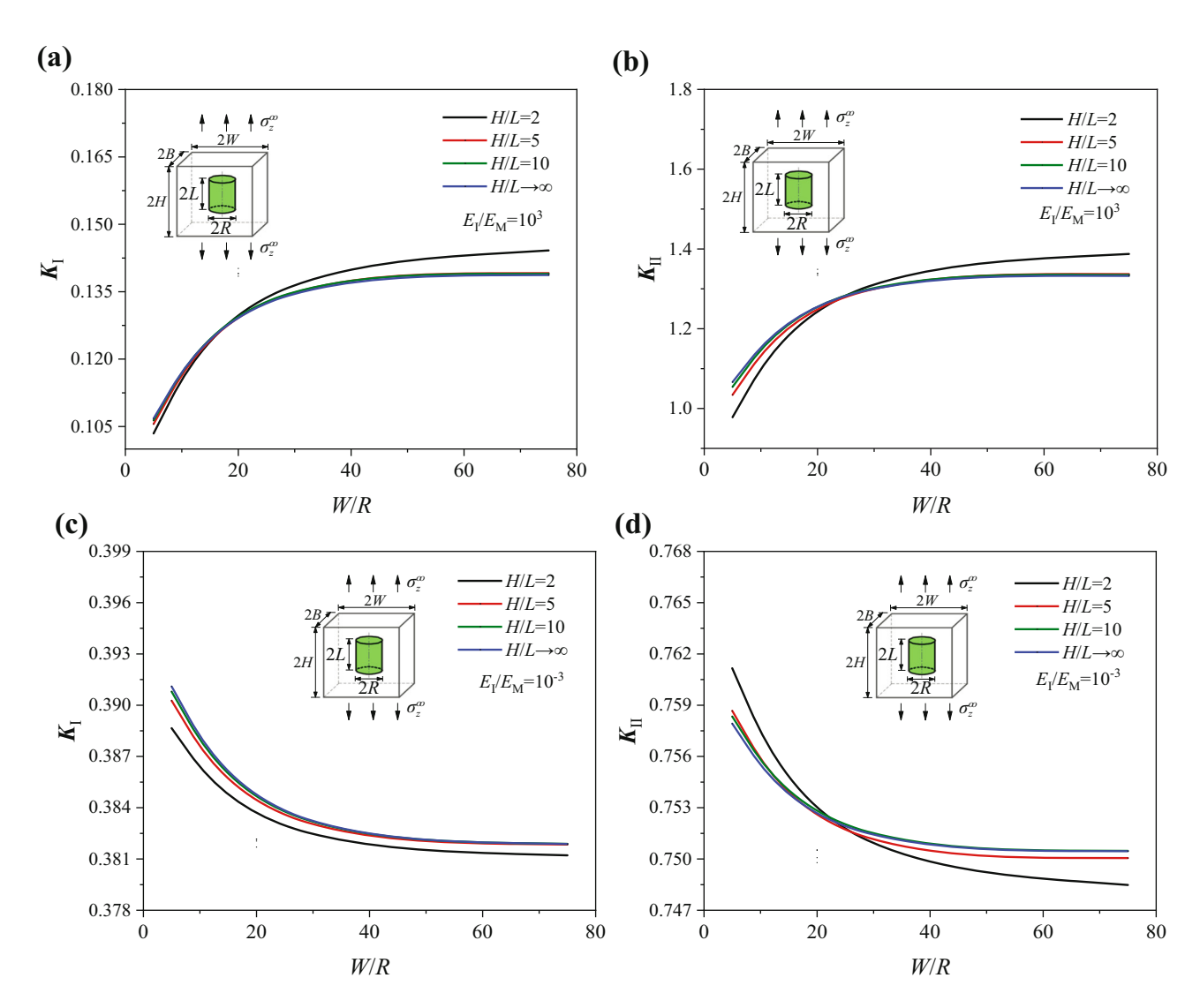


Figure 8: Effects of the unit cell size parameter W/R and the length-width ratio H/L on K_I and K_{II} under σ_z^{∞} : (a and b) $E_I/E_M = 10^3$ and (c and d) $E_I/E_M = 10^{-3}$, when L/R = 10; B = W.

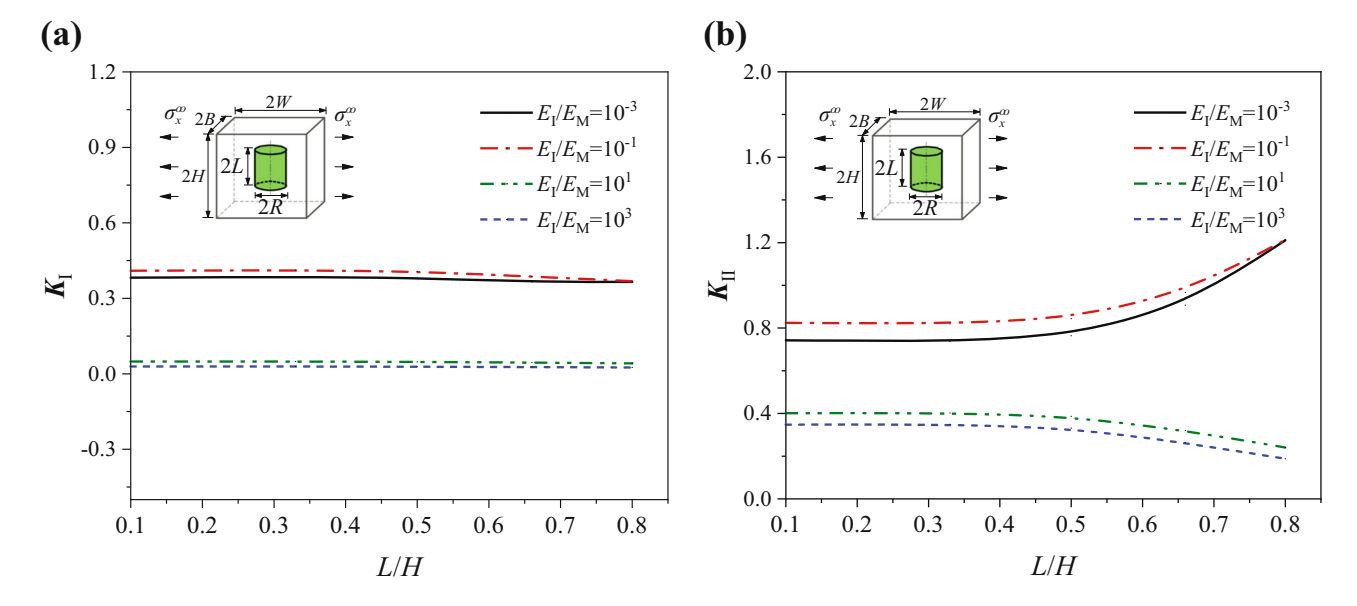


Figure 9: Variation in (a) K_{I} and (b) K_{II} with L/H of the unit cell (L/R = 1).

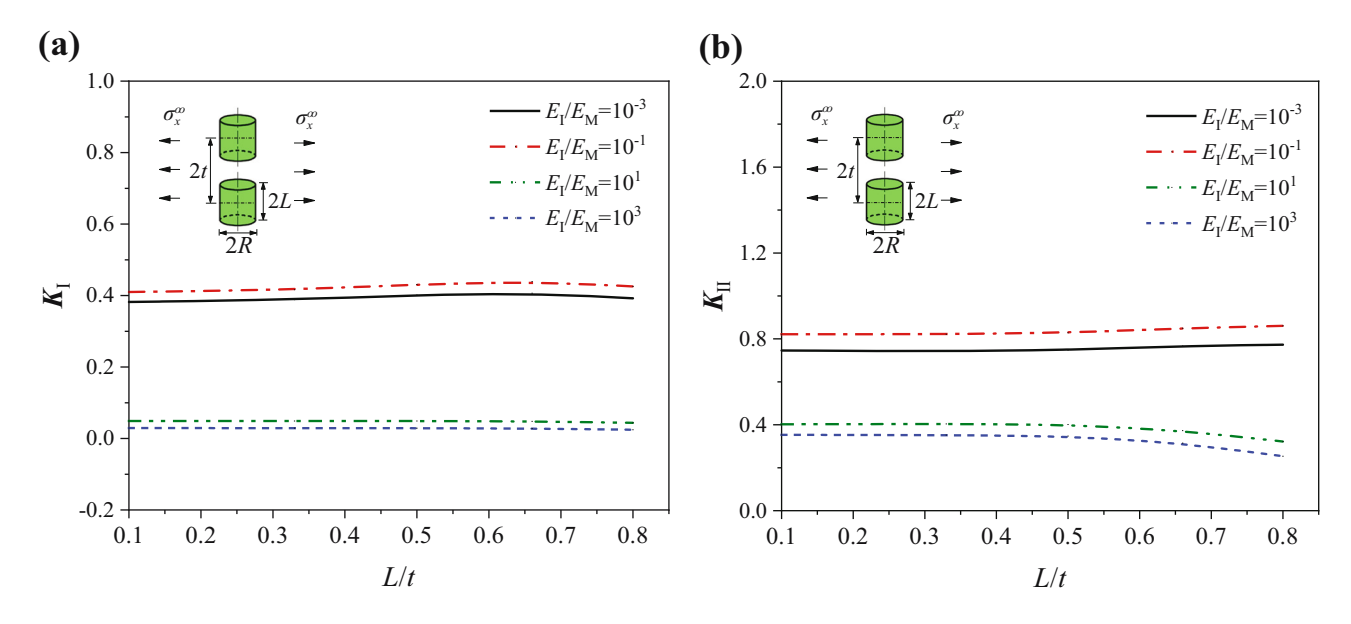


Figure 10: Variation in (a) K_{\parallel} and (b) K_{\parallel} with position parameter of the cylindrical inclusions (L/R=1).

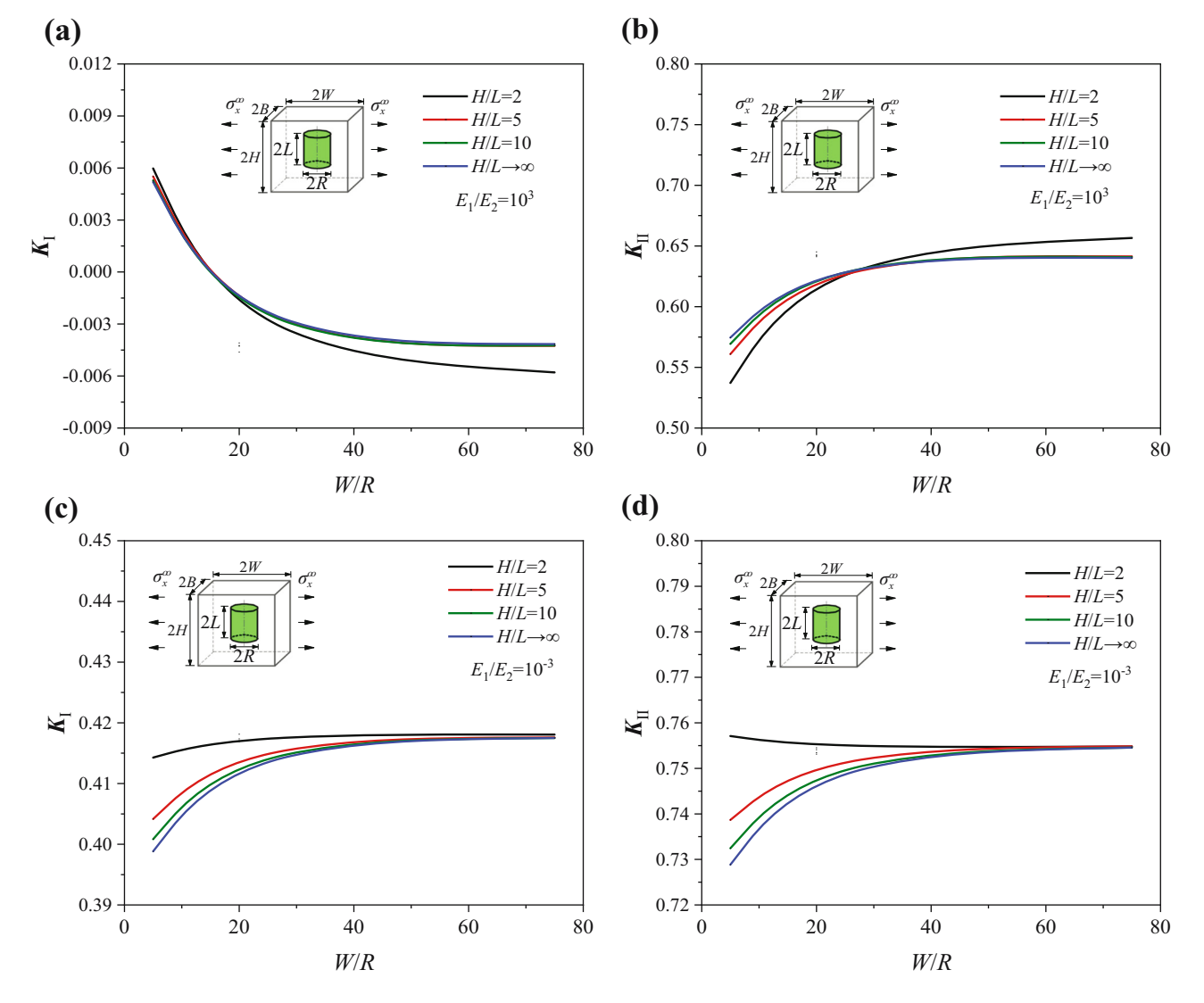


Figure 11: Effects of the unit cell size parameter W/R and the length-width ratio H/L on K_I and K_{II} under σ_X^{∞} : (a and b) $E_I/E_M = 10^3$ and (c and d) $E_{\rm I}/E_{\rm M}=10^{-3}$, when L/R=10.

 $E_{\rm I}/E_{\rm M}$ Change (%) F_{l} Change (%) F_{II} L/H (3D), l_1/l_2 (2D) 1/10 2/3 1/10 2/3 10^{-1} ЗD 0.288 0.253 -12.1531.904 2.276 19.538 10^{-1} 2D (20) 0.371 0.426 14.825 2.402 3.492 45.379 10 0.295 0.238 -19.322 0.616 0.477 -22.565 3D 10 2D (20) 0.229 0.182 -20.524 0.532 0.355 -33.271

Table 3: Comparison of SIFs between a cylindrical inclusion (3D) and a square inclusion (2D) under loading σ_z^{∞} (L/R=1)

Table 4: Comparison of SIFs between double cylindrical inclusion (3D) and double square inclusion (2D) aligned in the z-direction under loading σ_z^{∞} (L/R = 1)

E _I /E _M	F _I		Change (%)	F _{II}		Change (%)	
	L/t (3D), l_1/l_2 (2D)	1/10	2/3		1/10	2/3	
10 ⁻¹	3D	0.275	0.174	-36.727	1.843	1.719	-6.728
10^{-1}	2D (20)	0.324	0.179	-44.753	2.210	2.082	-5.792
10 10	3D 2D (20)	0.297 0.226	0.274 0.192	−7.744 −15.044	0.635 0.554	0.689 0.522	8.504 -5.776

5 Comparison between singular stress fields of the 2D and 3D models

The difference between the results of 3D cylindrical inclusion and 2D plane square inclusion is analyzed. Table 3 shows the dimensionless SIFs at the inclusion corner in a unit cell with different material properties and geometric sizes. The variation in the dimensionless SIFs at the 3D cylindrical inclusion corner and the 2D plane square inclusion corner with L/H (l_1/l_2) is basically the same, while there is a special case. In the range of $1/10 \le L/H$ $(l_1/l_2) \le 2/3$ and when $E_I/E_M = 10^{-1}$, F_I at the cylindrical inclusion corner decreased by 12.153%, while F_1 at planar square inclusion corner increased by 14.825%. Table 4 shows the dimensionless SIFs at the double square inclusion aligned in the z-direction. It is found that the variation trends of F_{II} in 3D hard inclusions with L/t (l_1/l_2) are different from that of 2D hard inclusions. In the 3D model, F_{\parallel} goes up by 8.504% with increase in L/H. On the other hand, in the 2D model, F_{II} goes down by 5.766% with increase in l_1/l_2 . As shown in Table 3, F_1 and F_{11} for 3D cylindrical inclusions are larger than that of 2D plane square inclusions when $E_{\rm I}/E_{\rm M}=10^{-1}$. $F_{\rm I}$ and $F_{\rm II}$ for 3D cylindrical inclusions are smaller than that of 2D plane square inclusions when $E_{\rm I}/E_{\rm M}=10^{1}$. This same rule applies to the double cylindrical inclusions aligned in the z-direction as shown in Table 4.

If 2D models are used to evaluate 3D results, their differences should be realized. The analysis results are conservative when $E_{\rm I}/E_{\rm M}=10^{-1}$, and the analysis results are dangerous when $E_{\rm I}/E_{\rm M}=10^{1}$.

6 Conclusion

The SICE model is established to analyze the fatigue strength parameters at the cylindrical inclusion corner in fiber-reinforced composites with local fiber discontinuity. The SIFs of a cylindrical inclusion and in the interaction of double inclusions aligned in the z-direction under tensile loadings in different directions in the unit cell are investigated. The effects of material properties, inclusion geometry and spacing, and unit cell size on SIFs were systematically discussed.

The present discussions show that the effect of the variation in volume ratio on the fracture mechanics properties of soft inclusions and hard inclusions is basically opposite. The sliding fracture effect of the distance between two inclusions on soft inclusions and hard inclusions is different.

The variations in unit cell size parameter and length-width ratio have an effect on SIFs. But when length-width ratio H/L > 10, the analysis results tend to be consistent.

Compared with the 2D models, the present analysis results are conservative for soft inclusions, and the analysis results are dangerous for hard inclusions.

The SICE method is effective to analyze the singular stress field at the cylindrical inclusion corner and provide references for the fatigue strength prediction and preparation of fiber-reinforced composites.

Acknowledgments: The authors acknowledge the support of the National Natural Science Foundation of China under grant No. 51975411 and the Tianjin Natural Science Foundation of China under Grant No. 18JCYBJC88500. Cong-Man Wang acknowledges the support of Tianjin Graduate Research and Innovation Project under grant No. 2020YISB072.

Funding information: The National Natural Science Foundation of China under Grant No. 51975411. The Tianjin Natural Science Foundation of China under Grant No. 18JCYBJC88500. Tianjin Graduate Research and Innovation Project under Grant No. 2020YJSB072.

Author contributions: Cong-Man Wang: writing – original draft, formal analysis, and visualization; Xue-Cheng Ping: methodology, writing - review and editing, and project administration; Xing-Xing Wang: writing - original draft, data curation, and investigation.

Conflict of interest: The authors declare that there is no conflict of interest regarding the publication of this article.

Data availability statement: All data generated or analyzed during this study are included in this published article.

References

- [1] Li LB. Damage and failure of fiber-reinforced ceramic-matrix composites subjected to cyclic fatigue, dwell fatigue and thermomechanical fatigue. Ceram Int. 2017;43(16):13978-96. doi: 10.1016/j.ceramint.2017.07.130.
- Deng Y, Li W, Wang X, Kou H, Zhang X, Shao J, et al. Temperature-dependent tensile strength model for 2D woven fiber reinforced ceramic matrix composites. J Am Ceram Soc. 2018;101:5157-65. doi: 10.1111/jace.15765.
- Sayyar M, Balachandra AM, Soroushian P. Energy absorption capacity of pseudoelastic fiber-reinforced composites. Sci Eng Compos Mater. 2014;21(2):173-9. doi: 10.1515/secm-2013-0021.
- Sun Z. Progress in the research and applications of natural fiber-reinforced polymer matrix composites. Sci Eng Compos Mater. 2018;25(5):835-46. doi: 10.1515/secm-2016-0072.

- Gu JF, Chen PH, Su L, Li K. A theoretical and experimental assessment of 3D macroscopic failure criteria for predicting pure inter-fiber fracture of transversely isotropic UD composites. Compos Struct. 2021;259:113466. doi: 10.1016/ j.compstruct.2020.113466.
- Ostapiuk M, Bieniaś J, Surowska B. Analysis of the bending and failure of fiber metal laminates based on glass and carbon fibers. Sci Eng Compos Mater. 2018;25(6):1095-106. doi: 10.1515/secm-2017-0180.
- Chen W, Ji X, Huang Z. Influence of fiber type on mechanical properties of lightweight cement-based composites. Sci Eng Compos Mater. 2021;28(1):249-63. doi: 10.1515/secm-2021-0021.
- Lazzarin P, Tovo R. A notch intensity factor approach to the stress analysis of welds. Fatigue Fract Eng M. 1998;21:1089-103. doi: 10.1046/j.1460-2695.1998.00097.x.
- Lazzarin P, Campagnolo A, Berto F. A comparison among some recent energy- and stress-based criteria for the fracture assessment of sharp V-notched components under Mode I loading. Theor Appl Fract Mec. 2014;71:21-30. doi: 10.1016/ i.tafmec.2014.03.001.
- [10] Seweryn A. Brittle fracture criterion for structures with sharp notches. Eng Fract Mech. 1994;47:673-81. doi: 10.1016/0013-7944(94)90158-9.
- Livieri P, Lazzarin P. Fatigue strength of steel and aluminium welded joints based on generalised stress intensity factors and local strain energy values. Int J Fract. 2005;133(3):247-76. doi: 10.1007/s10704-005-4043-3.
- Bogy DB, Wang KC. Stress singularities at interface corners in [12] bonded dissimilar isotropic elastic materials. Int J Solids Struct. 1971;7(8):993-1005. doi: 10.1016/0020-7683(71)
- [13] Zbib HM, Hirth JP, Demir I. The stress intensity factor of cylindrical cracks. Int J Eng Sci. 1995;33(2):247-53. doi: 10.1016/0020-7225(94)E0051-J.
- [14] Jiang CP, Xu YL, Cheung YK, Lo SH. A rigorous analytical method for doubly periodic cylindrical inclusions under longitudinal shear and its application. Mech Mater. 2004;36(3):225-37. doi: 10.1016/S0167-6636(03)00010-3.
- [15] Bian L, Chen L, Gao M. Stress distribution analysis and interface influence on fiber reinforced composites. Mech Mater. 2020;146:103400. doi: 10.1016/j.mechmat.2020.103400.
- [16] Mantič V. Interface crack onset at a circular cylindrical inclusion under a remote transverse tension. Application of a coupled stress and energy criterion. Int J Solids Struct. 2009;46(6):1287-304. doi: 10.1016/j.ijsolstr.2008.10.036.
- [17] Vable M, Maddi JR. Boundary element analysis of inclusions with corners. Eng Anal Bound Elem. 2007;31(9):762-70. doi: 10.1016/j.enganabound.2007.01.006.
- Chen DH. Analysis of singular stress field around the inclusion corner tip. Eng Fract Mech. 1994;49(4):533-46. doi: 10.1016/ 0013-7944(94)90047-7.
- Noda NA, Genkai T, Wang Q. Intensity of singular stress fields [19] at the end of a cylindrical inclusion. J Appl Mech. 2003;70:487-95. doi: 10.1115/1.1598479.
- [20] Noda NA, Takase Y, Hamashima T. Generalized stress intensity factors in the interaction within a rectangular array of rectangular inclusions. Arch Appl Mech. 2003;73(5/6):311-22. doi: 10.1007/s00419-002-0249-2.

- [21] Noda NA, Takase Y. Intensity of singular stress at the fiber end in a hexagonal array of fibers. Int J Solids Struct. 2005;42(16–17):4890–908. doi: 10.1016/j.ijsolstr.2005.01.021.
- [22] Bulling J, Gravenkamp H, Birk C. A high-order finite element technique with automatic treatment of stress singularities by semi-analytical enrichment. Comput Method Appl M. 2019;355:135–56. doi: 10.1016/j.cma.2019.06.025.
- [23] Tan MA, Meguid SA. Analysis of bimaterial wedges using a new singular finite element. Int J Fract. 1997;88:373–91. doi: 10.1023/A:1007427506134.
- [24] Liou WJ. Stress distributions of short fiber composite materials. Comput Struct. 1997;62(6):999-1012. doi: 10.1016/ S0045-7949(96)00307-0.
- [25] Madenci E, Shkarayev S, Sergeev B. Thermo-mechanical stresses for a triple junction of dissimilar materials: global-local finite element analysis. Theor Appl Fract Mec. 1998;30(2):103-17. doi: 10.1016/S0167-8442(98) 00047-0.
- [26] Lei YP, Wang H, Qin QH. Micromechanical properties of unidirectional composites filled with single and clustered shaped fibers. Sci Eng Compos Mater. 2018;25(1):143–52. doi: 10.1515/secm-2016-0088.
- [27] Zhang J, Katsube N. A hybrid finite element method for heterogeneous materials with randomly dispersed elastic inclusions. Finite Elem Anal Des. 1995;19(1-2):45-55. doi: 10.1016/0168-874X(94)00056-L.
- [28] Cai Z, Hu X, Yao W. Numerical study on bi-material interface crack using symplectic analytical singular element. Eng Fract Mech. 2018;199:308-26. doi: 10.1016/ j.engfracmech.2018.05.033.
- [29] Hu XF, Chen WH, Zhang P, Bui TQ, Yao WA. A new crack-tip singular element for cracks in three-dimensional elastic

- bodies. Eng Fract Mech. 2020;235:107148. doi: 10.1016/j.engfracmech.2020.107148.
- [30] Chen L, Liu GR, Jiang Y, Zeng K, Zhang J. A singular edge-based smoothed finite element method (ES-FEM) for crack analyses in anisotropic media. Eng Fract Mech. 2011;78(1):85–109. doi: 10.1016/j.engfracmech.2010.09.018.
- [31] Chen MC, Ping XC. A novel hybrid finite element analysis of inplane singular elastic field around inclusion corners in elastic media. Int J Solids Struct. 2009;46(13):2527–38. doi: 10.1016/j.ijsolstr.2008.08.030.
- [32] Ping XC, Chen MC, Xiao YH. Field intensity factors around inclusion corners in 0–3 and 1–3 composites subjected to thermo-mechanical loads. Int J Mech Mater Des. 2016:12(1):121–39. doi: 10.1007/s10999-014-9287-5.
- [33] Ping XC, Chen MC, Zhu W, Xiao YH, Wu WX. Computations of singular stresses along three-dimensional corner fronts by a super singular element method. Int J Comp Meth-Sing. 2016;14(6):1750065. doi: 10.1142/S0219876217500657.
- [34] Ping XC, Zhang YX, Guo YB, Xiao ZM, Jalde J, Chen MC. Intensity of stress singularity for the circumferential V-shape corner front of a three-dimensional diamond-like defect. Fatigue Fract Eng M. 2020;43(4):802–17. doi: 10.1111/ffe.13189.
- [35] Zhang YX, Ping XC, Wang CM, Xiao ZM, Yang JY, Chen MC. A new computational approach for three-dimensional singular stress analysis of interface voids. Acta Mech. 2021;232:639-60. doi: 10.1007/s00707-020-02842-0.
- [36] Sze KY, Wang HT. A simple finite element formulation for computing stress singularities at bimaterial interfaces. Finite Elem Anal Des. 2000;35(2):97-118. doi: 10.1016/S0168-874X (99)00057-8.
- [37] Chen MC, Sze KY. A novel hybrid finite element analysis of bimaterial wedge problems. Eng Fract Mech. 2001;68(13):1463-76. doi: 10.1016/S0013-7944(01)00015-7.